Effect of rolling on dissipation in fault gouges

F. Alonso-Marroquín*

*ESSCC, The University of Queensland, Qld. 4068, Brisbane, Australia and National Technical University of Athens,
5 Heroes of Polytechnion, 15773 Athens, Greece*

I. Vardoulakis

National Technical University of Athens, 5 Heroes of Polytechnion, 15773 Athens, Greece

H. J. Herrmann

*ICP, University of Stuttgart, Pfaffenwaldring 27, 70569 Stuttgart, Germany
and IfB, HIF E.11, ETH Hönggerberg, CH 8093 Zürich, Switzerland*

D. Weatherley and P. Mora

ESSCC, The University of Queensland, Qld. 4068, Brisbane, Australia

Sliding and rolling are two outstanding deformation modes in granular media. The first one induces frictional dissipation whereas the latter one involves deformation with negligible resistance. Using numerical simulations on two-dimensional shear cells, we investigate the effect of the grain rotation on the energy dissipation and the strength of granular materials under quasistatic shear deformation. Rolling and sliding are quantified in terms of the so-called *Cosserat rotations*. The observed spontaneous formation of vorticity cells and clusters of rotating bearings may provide an explanation for the long standing heat flow paradox of earthquake dynamics.

I. INTRODUCTION

The micromechanics of heat production by friction in granular materials has become an important issue in the study of earthquake mechanics. One of the unresolved controversies in this field is a phenomenon that geophysicists call the heat-flow paradox [1]. According to common sense, when two blocks grind against one another, there should be friction, and that should produce heat. However, measurements of heat flow during earthquakes are unable to detect the amount of heat predicted by simple frictional models. Calculations using the value of rock friction measured in the laboratory, i.e., a typical friction coefficient between 0.6 and 0.9 [2], lead to overestimation of the heat flux. As an example one refers in this context to the heat flow observations made around the San Andreas fault, which show that the effective friction coefficient must be around 0.2 or even less [3]. One possible scenario for the explanation of these observations is the mechanism of heat-induced pore-fluid pressure increase [3–5]. Other mechanisms have been also discussed [1,6,7]. At any rate, with or without pressurization, the correct assessment of frictional heat production during shear is a central issue. Here we will address this issue by resorting to the micromechanics of dry granular media representing the gouge, i.e., the shear band consisting of fragmented rock inside the fault zone.

The formation of rolling bearings inside the gouge has been introduced as a possible explanation for a substantial reduction of the effective friction coefficient [6]. This simplified picture assumes that the gouge is filled with more of less round grains which, as the plates move, can roll on each other thus reducing the amount of frictional dissipation. Granular dynamics simulations [1,8,9] and Couette experiments [10] have demonstrated the spontaneous formation of such bearings.

The overall effects of grain rotation are studied here using granular dynamics simulations. We show that particle rotation induces a phase separation in the granular media in terms of three coexisting phases: (1) vorticity cells, (2) rotational bearings, and (3) slip bands. The first two phases reduce significantly the frictional strength and the dissipation with respect to the hypothetical case of simple shear. We quantify these phases in terms of the so-called *Cosserat rotations*. We address the necessity to introduce these variables for the constitutive modeling of fault gouge. In Secs. II and III we present the theoretical background and the particle-based model. In Sec. IV the effect of particle rotation on the strength and frictional dissipation is investigated. In Sec. V we calculate the population of the three coexisting phases using the homothetic-antithetic decomposition of the Cosserat rotations.

II. COSSERAT CONTINUUM

In the framework of continuum mechanics, the mathematical description of granular rolling and sliding is a challenging task. We notice first that classical continuum theories introduce the concept of the material point as a representative assembly of grains and ascribes to it only the degrees of freedom of displacement, which in turn are correlated to the displacements of the grains of the assembly. Thus classical

___
*Electronic address: fernando@esscc.uq.edu.au

continuum theory makes no provision for particle rotation. More recent continuum models include the rotational degrees of freedom by using the so-called Cosserat rotations [11–14]. These are continuum field variables, measuring the relative particle rotations with respect to the rotational part of the displacement-gradient field. The name of these variables gives tribute to the brothers Cosserat (1909) who were the first to propose such a continuum theory. Fifty years after the first publication of the original work, the basic kinematics and static concepts of Cosserat continuum were reworked in a milestone paper by Günther [15]. Günther's paper marks the rebirth of micromechanics in the 1960s. Following this publication, several hundreds of papers were published on the subject of micromechanics of granular media [16]. The growing interest in the Cosserat theories in recent years followed the link that was made by Mühlhaus and Vardoulakis [14] between the Cosserat continuum and the onset of shear-bands in granular materials. Observations of particle rotations from particle-based and continuum-based computer models [17] and physical experiments [18] show that inside shear and interface bands the particles rotate differently as their neighborhood. These findings demonstrated the necessity to introduce the Cosserat rotations as additional field variables in the shear-band evolution. These new variables involved also a characteristic material length that allows in turn to reproduce the characteristic width of shear bands. This internal length has special significance from the computational point of view, because its resolves the mesh-dependency problems in the finite element simulations [19,20].

At any material point of the Cosserat continuum we assign a velocity $\vec{v}$ and a spin vector $\vec{\omega}$. Accordingly in plane-strain deformation the kinematic fields are: the classical strain-rate tensor, which corresponds to the symmetric part of the average particle velocity,

$$D_{ij} = \frac{1}{2}\left(\frac{\partial v_i}{\partial x_j} + \frac{\partial v_j}{\partial x_i}\right), \tag{1}$$

and the Cosserat rotation, that is given by the difference between the macrorotations and microrotations,

$$W = \frac{1}{2}\left(\frac{\partial u_x}{\partial y} - \frac{\partial u_y}{\partial x}\right) - \omega. \tag{2}$$

This variable can be calculated as the difference between the rotation of the branch vector—defined as the line connecting particle mass centers—and the rotation of the particle, averaged over all pair contacts in the representative volume element.

III. PARTICLE-BASED MODEL

We will investigate the discrete counterpart of the Cosserat rotations by using granular dynamics simulations. The discrete model consists of disks confined between two horizontal plates. A normal force is applied on the plates, as they are moved in opposite directions with a constant velocity. Periodic boundary conditions are imposed along the horizontal direction, see Fig. 1. This geometry is a simplified
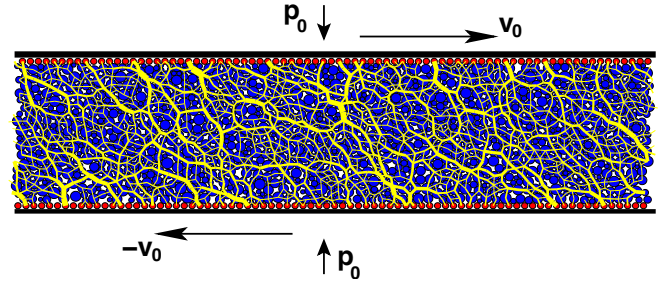

FIG. 1. (Color online) Contact network in the shear cell at critical state. The lines represent the branch vectors; the width of the lines, the normal contact force.

model of a gouge. Real rock gouge consists of nonspherical particles. In the present model we are able to simulate two extreme cases: The first one represents a young fault, which is characterized by a strong interlocking of closely packed rocks in the gouge. This case is simulated by hindering the rotation of the disks. In the second case we allow the particles to rotate without rolling resistance. This is an idealization of mature gouges, where the interlocking and the rock asperities are reduced due to grain fragmentation.

The discrete model is a two-dimensional (2D) implementation of the lattice solid model [1,21,22]. This is a suitable platform to investigate the dynamics of fault gouge via granular dynamics simulations. Two disks of radii R_i and R_j interact when the distance between their centers of mass r_{ij} is less that the sum of their radii. Their interaction is given by the viscoelastic contact force

$$\vec{f}^c = k_n \Delta x_n \vec{n} + k_t \Delta x_t \vec{t} + \delta_0 m(\gamma_n v_n^c \vec{n} + \gamma_t v_t^c \vec{t}). \tag{3}$$

The first two terms are elastic forces, and the last two are viscous forces. The unit normal vector $\vec{n}$ points in the direction of the vector connecting the center of mass of the two disks. The tangential vector $\vec{t}$ is taken perpendicular to $\vec{n}$. The elastic material constants are the normal k_n and tangential k_t grain contact stiffnesses. The normal elastic deformation is the overlapping length $\Delta x_n = R_i + R_j - r_{ij}$. The tangential elastic deformation is chosen to be consistent with the Coulomb sliding condition as follows: When two particles come into contact we set $\Delta x_t = 0$. Then, at each time t, we guess a new value for the tangential elastic deformation as

$$\Delta x_t^{\text{pred}}(t) = \Delta x_t(t - dt) + v_t^c dt, \tag{4}$$

where v_t^c is the tangential relative velocity at the contact,

$$v_t^c = \omega_i R_i + \omega_j R_j + (\vec{v}_i - \vec{v}_j) \cdot \vec{t}. \tag{5}$$

Here $\vec{v}_i$ is the velocity and ω_i is the angular velocity of the particles in contact. The predicted value of elastic deformation should be corrected to satisfy the Coulomb sliding condition $|f_t^e| < \mu f_n^e$, where f_t^e and f_n^e are the tangential and normal component of the elastic force and μ is the friction coefficient. This condition equates to

$$\Delta x_t(t) = \text{sgn}[\Delta x_t^{\text{pred}}(t)]\min\left(\frac{\mu k_n \Delta x_n(t)}{k_t}, |\Delta x_t^{\text{pred}}|\right). \quad (6)$$

The viscous force in Eq. (3) assures the restitution between colliding particles. γ_n and γ_t are coefficients of viscosity, and the harmonic mean $m = (1/m_i + 1/m_j)^{-1}$ is the effective mass of the disks. The normal and tangential components of the relative velocity at the contacts are $v_n^c = (\vec{v}_i - \vec{v}_j) \cdot \vec{n}$ and v_t^c given by Eq. (5). The factor $\delta_0 = \Delta x_n / R_0$ is included in Eq. (3), to guarantee continuity of the viscous force during collision. R_0 is the averaged radius of the disks.

The roughness of the driving plates is modeled by attaching particles to it. Their vertical displacement is controlled with a simple elastic force $f^b = k_n \delta$, where δ is the overlapping length. The attached disks are not allowed to rotate and their horizontal velocity is set to the velocity of the plates.

Each contact contributes to a direct force $\vec{f}^c$ and a torque $\tau^c = R_i \vec{f}^c \cdot \vec{t}$ in the equation of motions. The model does not include gravitational forces, but a viscous force $\vec{f}_i^v = \gamma m_i \vec{v}_i$ and a torque $\tau = \gamma m_i R_i^2 \omega_i$ is included for each particle. This viscous forces allow relaxation of particles without contacts. We use the Verlet method for solving the equations of motion [23].

The efficiency of the simulation is mainly determined by the method of contact detection. Our method searches in each step the contacts in a list of *neighbors* that is called a Verlet list. This list is constructed by taking the pair particles whose distance of their center of mass satisfies the constraint $r^{ij} < R_i + R_j + \delta$. The Verlet list is updated when the maximal displacement of the particles since the last update is larger than $\delta/2$. The parameter δ is chosen by making a compromise between the storage (size of the Vertex list) and the compute time (frequency of list updates). A linked cell algorithm is used to allow a rapid calculation of the new Verlet list [24].

The material constants of the model are the normal stiffness $k_n = 1$; the tangential stiffness $k_t = 0.1$; the normal $\gamma_n = 0.001$ and tangential $\gamma_n = 0.0001$ damping frequency and the body viscosity $\gamma = 0.0001$. The density of the disks $\rho = 1$; and the friction coefficient whose default value is $\mu = 0.5$. The control parameters are the applied pressure $p_0 = 0.001$, and the velocity of the plates $v_0 = 10^{-6}$. The time step is $\Delta t = 0.05$. The most relevant parameter of this model is the ratio between the shear velocity v_0 and the velocity of compressional waves, which in our model is $v_p \sim R_0 \sqrt{k_n/m}$. In our simulation $v_p \sim 1$ so that $v_p/v_0 \sim 10^6$. This value should be compared to the ratio in realistic fault zones, where $v_p \sim 1$ km/s and $v_0 \sim 1$ cm/year leading to a factor of $v_p/v_0 \sim 10^{10}$. To remedy this discrepancy of time scales we use the quasistatic limit: The velocity is chosen low enough so that the reduction of it by one-half affects the effective friction coefficient by less than 5%.

IV. EFFECT OF PARTICLE ROTATION

Here we address the question of how particle rotation affects the mechanical response of the shear cell. Simulation of shear cells with rotating and nonrotating disks are compared
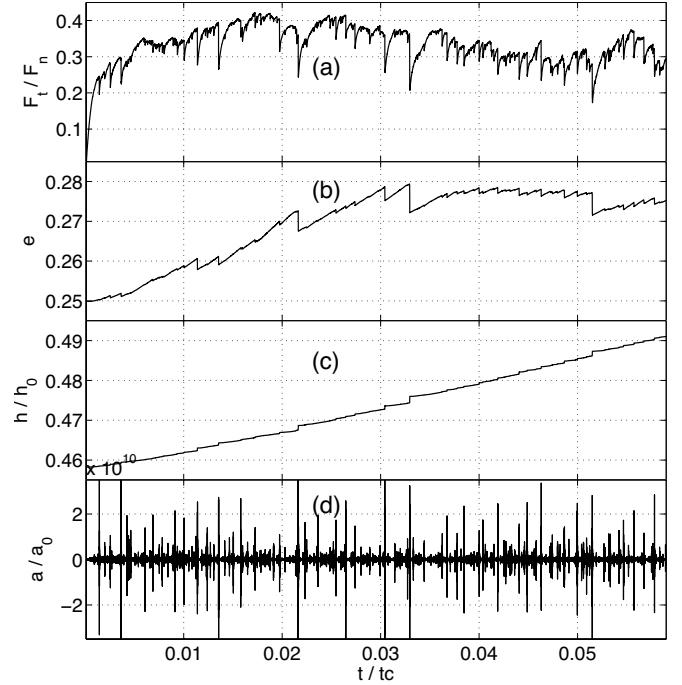

FIG. 2. Time profiles of (a) ratio between the normal and tangential force acting on the plates, (b) void ratio, calculated as $e = (A - A_d)/A_d$, where A is the area of the cell and A_d is the total area occupied by disks, (c) frictional dissipation normalized by $h_0 = L p_0 v_0 t_c$ and (d) acceleration of one disk in the center of the cell, normalized by $a_0 = L/t_c^2$. The time is normalized by $t_c = L/v_0$.

by calculating the power dissipation and the stress ratio at the limit of large shear deformation. Each shear cell consists of 1600 disks with random sizes between $0.5R_0$ and $1.5R_0$. The length of the cells is $80R_0$. We start from a loose packing that is compressed by applying a constant pressure at the top plate. After a short collisional regime the sample reaches an equilibrium configuration where the kinetic energy decreases exponentially with time. After this stage the sample is sheared by applying a horizontal velocity v_0 at the top plate and $-v_0$ at the bottom. The simulations are performed by taking microscopic friction coefficients between 0.0001 and 8. These values should be compared with the friction of realistic materials, which ranges from 0.0001 for superlubricated surfaces to 1.2 for rubber-concrete contact surfaces.

All samples reach a limit state for large shear deformation. This state resembles the so-called critical state of soil mechanics [25]. As shown in Fig. 2, the stress and the void ratio reach a constant value besides some fluctuations. These fluctuations result from the characteristic stick-slip dynamics of the shear cell: In the stick phase, the elastic energy is stored in force chains. These chains build up during the slow relative motion of the plates. The elastic energy is released in form of *quakes*. Each quake corresponds to the collapse of a force chain which is reflected by an abrupt drop of the macroscopic stress and a sudden compaction of the sample. The collapse of force chains leads to reorganization of the particles and hence acoustic emission. This is detected from the acceleration of a single particle in the sample, see part (d) of
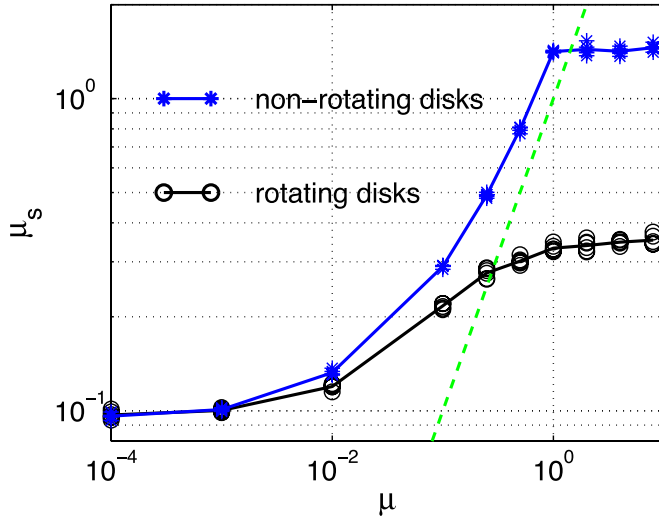
FIG. 3. (Color online) Dependence of the effective friction coefficient (μ_s) on the microscopic friction coefficient for rotating and nonrotating particles. Data of five different samples are superposed. Solid lines represent the linear interpolation around the averaged value. Dashed line corresponds to $\mu_s = \mu$.

Fig. 2. Between two quakes the buckling of forces chains leads to an overall elastoplastic response with constant increase of void ratio.

A. Macroscopic coefficient of friction

The instantaneous strength of the shear cell in the critical state can be quantified by an effective friction coefficient $\mu^* = F_t / F_n$. Here F_n and F_t are the normal and tangential force acting on the top plate. Part (a) of Fig. 2 shows the time evolution of μ^*. Typically this value increases in the interval between two quakes, and it drops during the quakes, leading to time fluctuations which are of the same order as the time average value.

We define the macroscopic friction coefficient as the time average of μ^* over the critical state,

$$\mu_s = \langle \mu^* \rangle = \frac{\langle F_t \rangle}{F_n}. \tag{7}$$

The dependence of μ_s on the microscopic friction coefficient for rotating and nonrotating disks is plotted in part (a) of Fig. 3. For small values of μ the strength of the shear cells is not affected by grain rotation. In both cases the effective friction coefficient is larger than μ. In the limit case $\mu \to 0$ the effective friction tends to 0.1. This shows that interparticle friction is not the only origin of the macroscopic frictional behavior of granular materials.

For large values of μ particle rotation has a significant effect on the strength of the shear cell. Particularly, in the range $0.28 < \mu < 1.42$ samples with rotating disks have a macroscopic friction coefficient lower than the contact friction coefficient. On the other hand, the macroscopic friction coefficient is larger than the contact friction coefficient for nonrotating disks. In the limit $\mu \to \infty$, the strength of both

samples tends to a constant value. This value is 0.34 for rotating disks samples and 1.43 for nonrotating disks.

B. Energy dissipation

We now turn to the effect of grain rotation on dissipation. Energy loss in the sample results from frictional and viscous dissipation. Therefore the produced heat can be calculated as

$$h = \int P(t)dt, \tag{8}$$

where P is is the amount of work per unit of time done by the dissipative forces. This can be decomposed as

$$P(t) = P_f(t) + P_v(t), \tag{9}$$

P_f and P_v being the frictional and viscous power dissipation. The first quantity is calculated as the sum of the tangential force times the sliding velocity of all the contacts,

$$P(t) = \sum_c f_t^e \left(v_t^c - \frac{d(\Delta x_t^c)}{dt} \right), \tag{10}$$

where f_t^e is the tangential elastic contact force; v_t^c the tangential relative velocity at the contact, and Δx_t^c the elastic part of the tangential displacement as defined by Eq. (6). The second term in Eq. (8) is given by

$$P_v(t) = \sum_c \delta_0 m [\gamma_n(v_n^c)^2 + \gamma_t(v_t^c)^2] + \sum_p \gamma m_i(v_i^2 + R_i^2 \omega_i^2), \tag{11}$$

where the first sum goes over the viscous dissipation of all contacts, and the second one over the dissipation of the viscous body forces of all particles.

The heat versus time is plotted in part (c) of Fig. 2 for rotating particles with $\mu = 0.5$. The general trend of the heat is to increase slowly between two quakes, and rapidly during quakes. The contribution to heat during two quakes is almost frictional dissipation, but at the quakes there is a non-negligible contribution of viscous dissipation. The power dissipation, which is given by the derivate of the heat, fluctuates in time around a constant value. In the Appendix we show that this value relates to the macroscopic friction coefficient as

$$\langle P(t) \rangle = \mu_s F_n v_t, \tag{12}$$

where μ_s is the macroscopic friction coefficient defined in Eq. (7), F_n the normal force on the plates, and $v_t = 2v_0$ the relative shear velocity of the plates. Replacing Eq. (9) into this equation, we decompose the macroscopic friction as

$$\mu_s = \mu_f + \mu_v, \tag{13}$$

where μ_f and μ_v are the contribution to dissipation by the frictional and viscosity forces,

$$\mu_f = \frac{\langle P_f(t) \rangle}{F_n v_t}, \quad \mu_v = \frac{\langle P_v(t) \rangle}{F_n v_t}. \tag{14}$$

The dependency of the frictional and viscous power coefficients on μ is shown in Fig. 4. For small values of μ they are
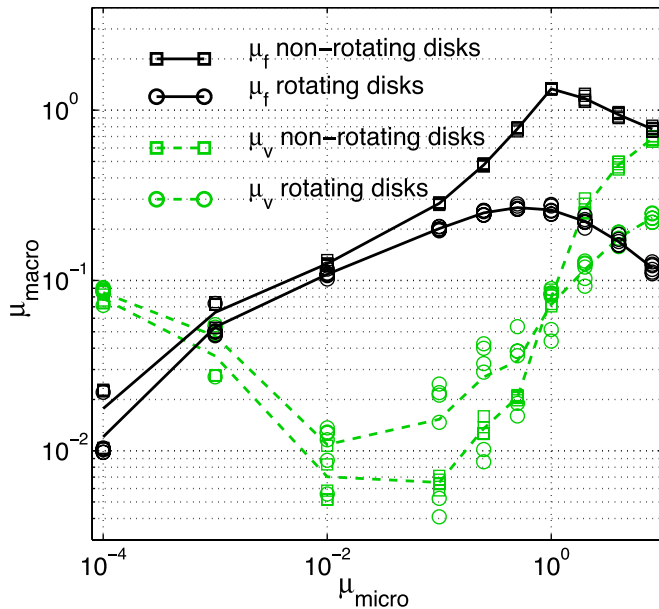
FIG. 4. (Color online) Dependence of the viscous power coefficient (μ_v) and frictional power coefficient (μ_f) on the microscopic friction coefficient for rotating and nonrotating particles. Data of five different samples are superposed. Lines represent the linear interpolation around the averaged value.

FIG. 5. (Color online) Simple shear model of gouge deformation.

not affected by particle rotation. On the other hand, when the microscopic friction coefficient is rather large, rotation reduces the power frictional dissipation in almost one order of magnitude. Frictional dissipation peaks at $\mu=0.5$ for rotating particles and $\mu=1.0$ for nonrotating particles. Frictional dissipation decreases as $\mu \to 0$ and $\mu \to \infty$. In the first case because $f_t \to 0$ and in the second case because the fraction of sliding contacts is very small for large microscopic friction coefficients.

As a result of stick-slip instabilities, there is a significant amount of energy dissipation due to collisions. In the limit $\mu \to 0$ viscosity is the dominant mechanism of strength and energy dissipation. Viscous dissipation is also significant for large values of μ, due to the large stick-slip instabilities which characterize this regime.

C. Displacement field

The origin of strength and frictional dissipation in the shear cell should be associated to the deformation patterns inside the cell. The simplest deformation picture is the so-called simple shear. As shown in Fig. 5, this model corresponds to the shear of a multilaminate with interlaminate friction equal to μ. Macroscopic friction coefficients larger that the microscopic one can be explained by the addition of interlocking between the layers. However, this picture does not provide explanation to macroscopic friction coefficients lower that the microscopic one.

In the context of heat flow paradox, it has been pointed out that the picture of simple shear is not complete unless one considers particle rotation [1]. It is believed that the shear stress in the rocks of the gouge will reduce the shape irregularities that hinder the rocks to rotate. Subsequent shear
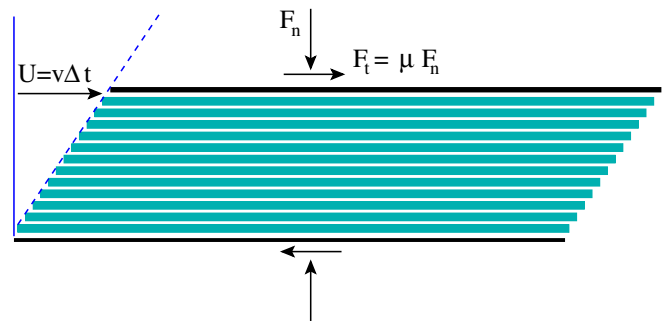
will therefore induce particle rotations which reduces considerably the frictional dissipation with respect to the expected value of simple shear.

In order to verify this hypothesis, we compare the displacement field of shear cell with rotating and nonrotating disks. In part (a) of Fig. 6 we plot the displacement field for nonrotating particles when $\mu=0.5$. We observe the formation of blocks of particles moving approximately as a whole. The boundaries between these blocks are not flat, but curved. This produces strong interlocking, that explains the considerable increase of the strength of the material with respect to simple shear. Note that these blocks cannot slide against each other for very long without changing shape. The reorganization of these structures appears by means of large quakes. These quakes change completely the displacement fields, even when the position of the particles stays approximately the same.

If the particles are allowed to rotate, vorticities appear spontaneously. They are shown in part (b) of Fig 6. These vorticities are accompanied by strong temporal fluctuations
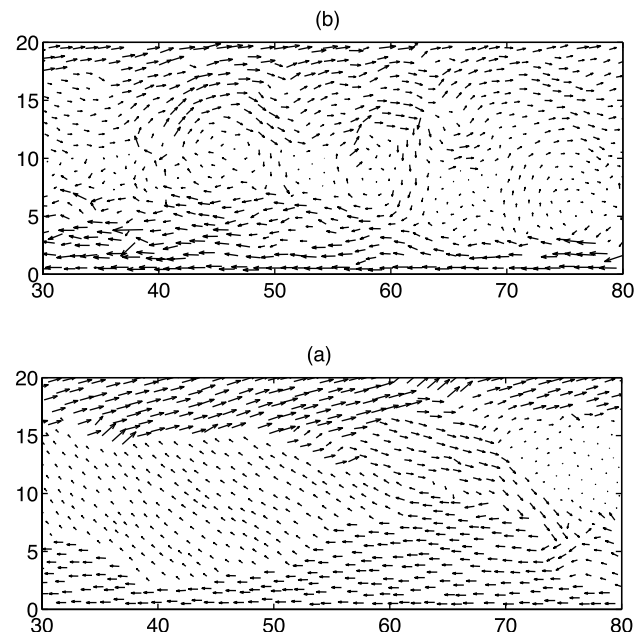

FIG. 6. Snapshot of the velocity field for (a) nonrotating and (b) rotating grains. The friction coefficient is $\mu=0.5$.

of the displacement field, but they can appear and disappear intermittently in the same zone. The vorticity field has been observed in many numerical simulations [26,27]. It resembles to some extent the turbulent regime observed in fluids, but their dynamics is quite different [28]: Fluids under slow motion present a laminar regime where the mass displacements can be considered as simple shear. On the other hand, our shear cells develop large vorticities even in the quasistatic regime, ruling out the simple shear deformation regime. The short lifetime of these vorticities, typically the same as the interval between two large quakes, contrasts to the large lifetime of the eddies in turbulent flow. Thermal measurements in dynamic shear banding on metals also reveals that homogeneous shear is not possible and vortices are the rule [29].

The spatial distribution of vorticity cells, when combined with the distribution of rolling, provides a picture of the bearings: Inside vorticity cells all particles rotate as a rigid body, whereas the space between the vorticity cells is characterized by intense relative rotations. This leads to clusters of rotational bearings and zones of intense slippage. We will quantify the contribution of these modes to global deformation by performing a kinematic decomposition of the contact deformation. This decomposition will distinguish rolling from sliding and from the rigid body motion of the vorticity cells.

V. MEASURE OF ROLLING

Several definitions of rolling can be found in the literature [30–32]. They are taken as measures of contact deformation for each pair of interacting particles. Kuhn and Bagi decompose the degrees or freedom of the two particles into rigid body motion and objective motion [31]. Then the rolling is defined as the average of the objective translation at each side of the contact point [32]. Based on these studies, we introduce a definition of rolling in terms of the rotation and translation of the particles in contact. This definition will be consistent with the fact that rolling allows deformation in the assembly without frictional dissipation or accumulation of elastic energy.

Let us suppose that at time t two particles indexed by i and j are in contact, and they stay in contact during an infinitesimal time interval dt afterward. We introduce a system of coordinates $\vec{n}^{ij}$, $\vec{t}^{ij}$, $\vec{z}^{ij}$ attached to the contact. The unit normal vector $\vec{n}^{ij}$ connects the center of mass of the particle i to that of the particle j,

$$\vec{n}^{ij} = \frac{\vec{x}_j(t) - \vec{x}_i(t)}{|\vec{x}_j(t) - \vec{x}_i(t)|} \approx \frac{\vec{x}_j(t) - \vec{x}_i(t)}{R_i + R_j}. \tag{15}$$

The latter approximation is valid when $\Delta x_n \ll d$, where Δx_n is the overlapping length and d the characteristic diameter of the disks. The unit vector $\vec{z}^{ij}$ is perpendicular to the plane of the disks, and the unit tangential vector satisfies $\vec{t}^{ij} = \vec{z}^{ij} \times \vec{n}^{ij}$.

Let us consider two points attached to each particle, in a region infinitesimally near to the contact point. The tangential velocity of these points are given in terms of the linear $\vec{v}_k$ and angular ω_k velocities of the particles,

$$v_{i,t}^c = \vec{v}_i \cdot \vec{t} + \omega_i R_i, \quad v_{j,t}^c = \vec{v}_j \cdot \vec{t} - \omega_j R_j. \tag{16}$$

Let us take the movement of the branch vector. That is, the vector connecting the center of mass of the two particles. The position of the point attached to the branch vector at the contact is $\vec{C} = \vec{x}_i + R_i \vec{n}^{ij}$. We define *rigid body velocity* as the tangential component of the velocity of this point. According to Eq. (15), this velocity is given by

$$V_{rb}^{ij} = \frac{(\vec{v}_i R_j + \vec{v}_j R_i) \cdot \vec{t}}{R_i + R_j}. \tag{17}$$

If the two particles move as a rigid body, the velocity coincides with Eqs. (16). Otherwise there is a relative velocity between the two points attached to the particles. This velocity can be calculated by subtracting the rigid body like velocity of Eq. (17) from the contact velocities of Eqs. (16),

$$s^{ij} = v_{i,t}^c - V_{rb}^{ij}, \quad s^{ji} = v_{j,t}^c - V_{rb}^{ij}. \tag{18}$$

These velocities can be given in terms of linear and angular velocities by using Eqs. (16) and (17),

$$s^{ij} = \omega_i R_i - \frac{R_i}{R_i + R_j}(\vec{v}_j - \vec{v}_i) \cdot \vec{t}^{ij},$$

$$s^{ji} = -\omega_j R_j + \frac{R_j}{R_i + R_j}(\vec{v}_j - \vec{v}_i) \cdot \vec{t}^{ij}. \tag{19}$$

They will be called *objective velocities* of the two particles at the contact. These velocities are *objective* in the sense that their magnitude is unaffected by the common rigid-body motion of the particle pair. In particular, these measures are not affected by a change of the reference frame. The objective velocities vanish if, and only if, the two particles move as a rigid body. Otherwise the objective velocities involve rolling, sliding or accumulation of shear strain at the contact.

We will relate these *objective velocities* to the aforementioned Cosserat-continuum rotations. At the micromechanical level, the latter are defined as the relative rotation of the particle with respect to the rotation of the branch vector around the axis parallel to $\vec{z}^{ij}$ at the contact point [33]:

$$W^{ij} = \omega_i - \Omega^{ij}, \quad W^{ji} = \omega_j - \Omega^{ij}, \tag{20}$$

where ω_i is the angular velocity of the particle i with radius R_i. Ω^{ij} is the rotational velocity of the branch vector,

$$\Omega^{ij} = \frac{(\vec{v}_i - \vec{v}_j) \cdot \vec{t}^{ij}}{R_i + R_j}. \tag{21}$$

Replacing Eq. (21) into Eqs. (20) and comparing the result with Eqs. (19), we obtain a relation between the Cosserat rotations and the objective velocities.

$$s^{ij} = R_i W^{ij}, \quad s^{ji} = -R_j W^{ji}. \tag{22}$$

These equations provide an interesting connection between the relative orientation of the Cosserat rotation and rolling: When the Cosserat rotations are in a *homothetic couple* as shown in part (a) of Fig. 7, the objective velocities s^{ij} and s^{ji} have opposite signs. In this case, depending on whether the contact is or not in the sliding condition, the
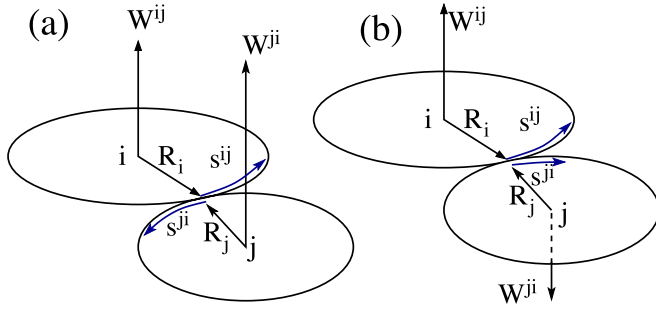
FIG. 7. (Color online) Homothetic (a) and antithetic (b) couple of the Cosserat rotations.

contact deformation results either in frictional dissipation or in accumulation of elastic energy, without rolling deformation. Homothetic couples appear in several cases: If the two disks in contact rotate in the same sense without linear velocity, the Cosserat rotations reads $W^{ij} = \omega_i$ and $W^{ji} = \omega_j$. If the particles do not rotate, the Cosserat rotations are given by $W^{ij} = W^{ji} = \Omega^{ij}$. In both cases they are in a homothetic couple, and hence there is no rolling deformation.

The appearance of rolling between the particles is linked to the *antithetic couple* of the Cosserat rotations. This couple is shown in part (b) of Fig. 7. In this case the rolling is given by the common part of the objective velocities, i.e., $\min(|s^{ij}|, |s^{ji}|)$. In particular, if the Cosserat rotations satisfy $W_i R_i + W_j R_j = 0$ both grains have the same objective velocity. Therefore the contact deformation does not accumulate elastic deformation or produce frictional dissipation, and hence the deformation corresponds to pure rolling.

In the general case the objective velocities should be decomposed into rolling and dislocation. The first one results in

$$V_{\text{roll}}^{ij} = \begin{cases} 0 & \text{homothetic couple,} \\ \min(|s^{ij}|, |s^{ji}|)\text{sgn}(s^{ij}) & \text{antithetic couple,} \end{cases}$$

$$\tag{23}$$

and the dislocation is given by the difference of the objective velocities,

$$V_{\text{dis}}^{ij} = s^{ij} - s^{ji}. \tag{24}$$

Using the identity $s^{ij} - s^{ji} = v_{i,t}^c - v_{j,t}^c$, it is easy to prove that the dislocation velocity corresponds to the relative tangential velocity defined in Eq. (5). In the limit of rigid disks, where elastic deformation at the contact is absent, the dislocation velocity coincides with the sliding velocity. In granular dynamics an elastic shear deformation is allowed, so that the sliding velocity is given by

$$V_{\text{slid}}^{ij} = V_{\text{disl}}^{ij} - \frac{d(\Delta x_t)}{dt}, \tag{25}$$

where Δx_t is the elastic part of the tangential displacement at the contact, that is given by Eq. (6). According to Eq. (9) the sliding velocity times the tangential force corresponds to the frictional dissipation. The second term of Eq. (25) involves accumulation of elastic energy.

The Cosserat rotations turn out to be a suitable *order parameter* to describe the vorticities and bearings in the shear deformation: As shown in Fig. 8, the spatial distribution of these structures is not just random, but strong correlations appear in form of three coexisting phases: (1) Vorticity cells, where the particles rotate almost as a whole, so that the Cosserat rotation is vanishingly small, (2) clusters of particles with intense rolling (rotational bearings), where the Cosserat rotations are antithetic, and (3) zones between particles with intense dislocation (microbands), characterized by
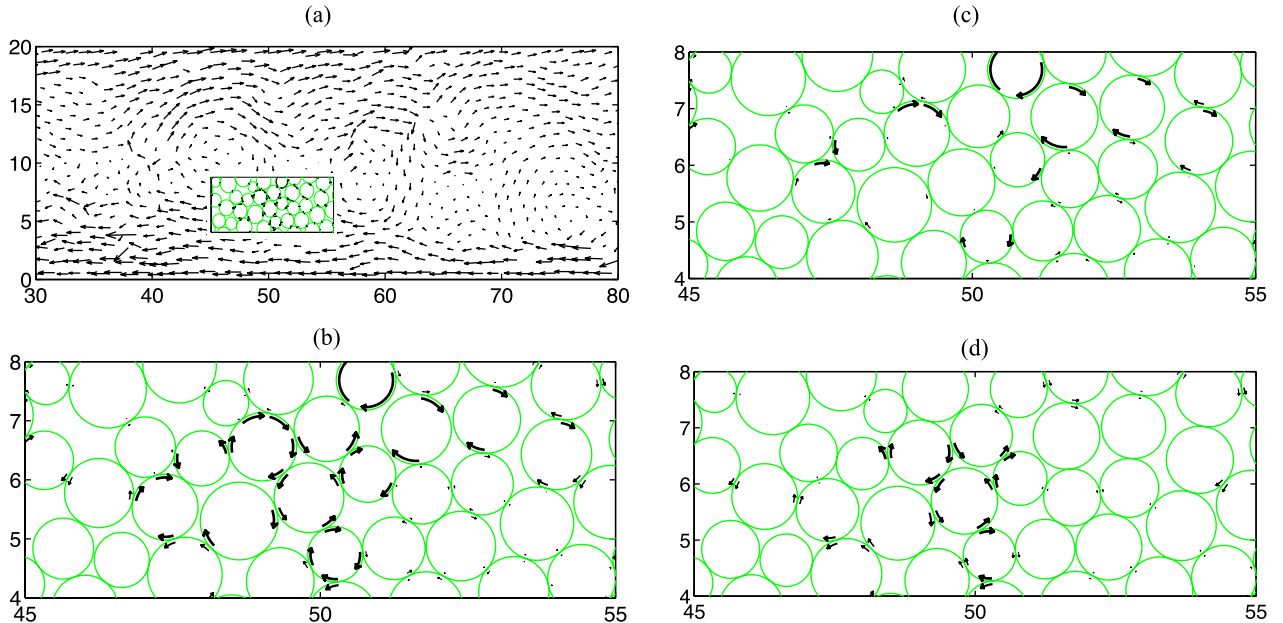

FIG. 8. (Color online) Snapshot of (a) vorticity field, (b) objective velocities at the contacts as shown in the inset of part (a), and their decomposition in (c) dislocation and (d) rolling. The sample consists of rotating grains with $\mu = 0.5$.
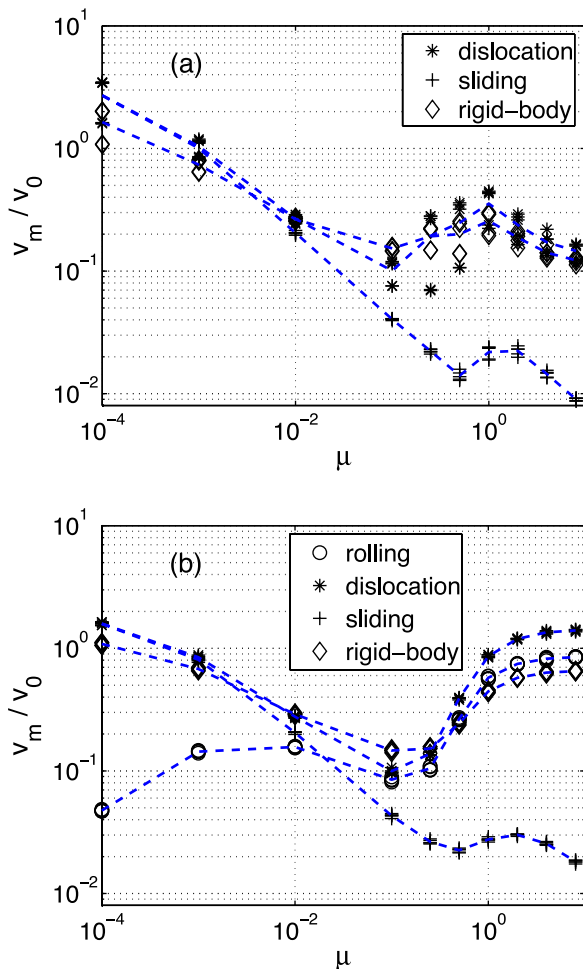
FIG. 9. (Color online) Decomposition of kinematic roles for (a) nonrotating and (b) rotating particles, as function of μ. They are calculated from the average of the absolute value of the rolling, dislocation, sliding, and rigid-body velocities at the contacts. Data of five different samples are superposed.
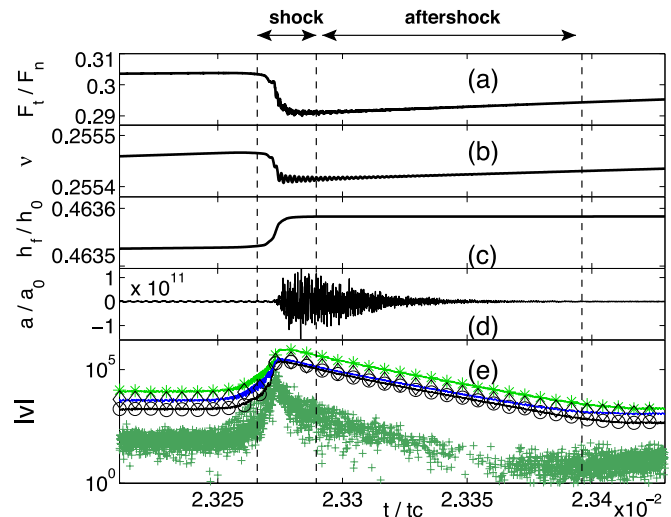

FIG. 10. (Color online) Time evolution of (a) stress, (b) void ratio, (c) frictional dissipation, and (d) acoustic emission at the center of the sample. (e) Average of the absolute value of rolling (circles), dislocation (asterisks), sliding (crosses), and rigid-body velocities (diamonds). The sample consists of rotating particles with $\mu=0.5$.

homothetic couples of the Cosserat rotations. Microbands induce frictional dissipation and accumulation of elastic energy, whereas the rotational bearings accommodate the vorticity cells to make them more compatible with the imposed kinematic boundary conditions.

The microscopic friction coefficient can serve as a control parameter of the relative population of these three phases. This is shown in Fig. 9 for (a) nonrotating and (b) rotating particles. In both cases the sliding displacement and rigid-body velocities are the dominant deformation modes for small values of μ. In this regime, the dislocation velocity coincides with the sliding velocity, because almost all the contacts are in the sliding condition. Deformation in this case is characterized by small clusters of particles moving against each other through microbands of intense sliding. For rotating particles the rolling is much lower than the other deformation modes, whereas the rolling is absent for nonrotating grains.

For large friction coefficients the sliding velocity becomes negligible, because few contacts are able to reach the sliding condition. In this regime, depending on whether the particles

are or not allowed to rotate, the population of the deformation modes is quite different: for nonrotating particles, the contact deformation is dominated by rigid-body motion and elastic dislocation. The latter one builds up elastic energy that is liberated in the form of strong quakes. The dependence of dislocation and rigid-body motion on μ is fairly weak. This reflects a self-organization of the shear cells, characterized by a nondependency of the effective friction coefficient on μ, already shown in Fig. 3.

For rotating grains and large friction coefficients rolling plays a relevant role, as shown in part (b) of Fig. 9. The deformation is dominated by rigid-body motion (due to the vorticities), rolling (due to the rotational bearings) and elastic dislocation (due to building of force chains). The self-organization of the shear cells is given by the fact that rolling and vorticities are not affected by a change in the microscopic friction coefficient. The sliding turns out to be much smaller that the other modes, because only few contacts can reach the sliding condition. Therefore the dislocation results almost completely in accumulation of elastic energy that is released in the form of quakes.

The details of the dynamics of one quake is shown in Fig. 10. We use a friction coefficient of $\mu=0.5$. We observe a small time interval (shock) characterized by a sudden decrease of the effective friction coefficient, along with an abrupt compaction and a rapid frictional dissipation. This is followed by a longer time interval (aftershock) given by an exponential decay of microseismic activity with almost no frictional dissipation. More details of the structure of the quake are visible by calculating the time evolution of the contact modes of deformation. Part (e) of Fig. 10 shows that most of the contact deformation at the shock corresponds to rolling and rigid-body deformation. In the aftershock the sliding velocities become vanishing small, whereas the other modes decay exponentially. Acoustic waves are generated at

the point where the force chain fails. These waves travel though the sample and they are reflected as they reach the plates. After many reflections they become uncorrelated, which removes almost all contacts from the sliding condition. Therefore sliding velocity modes are not active in the aftershock, whereas the other modes decay exponentially in the form of uncorrelated oscillations.

As far as earthquakes are concerned, it is remarkable that only a minute part of the contact deformation during the quake corresponds to sliding. This leads to an effective friction coefficient around 0.25 which is lower than the contact friction coefficient of $\mu = 0.5$, see Fig. 3. Therefore the introduction of rolling in the gouge dynamics could potentially explain the low friction of faults and low stress drops during earthquakes.

VI. CONCLUDING REMARKS

The most important contribution of this work is to show that spontaneous formation of vorticity cells assisted by rotational bearings is the mechanism of reduction of strength and frictional dissipation in shear cells. For the range of rock friction of $\mu = 0.6 - 0.9$, the effective friction coefficient increases from $\mu_s = 0.3$ to $\mu_s = 0.35$, whereas the frictional power coefficient decreases from $\mu_f = 0.28$ to $\mu_f = 0.22$. These results are consistent with previous numerical simulations [1] and heat flow observations in fault gouges [3], where the effective coefficient of friction is around one order of magnitude lower than the contact friction coefficient. The existence of such rotational patterns confirm earlier speculations about the origin of this reduction of friction.

The strong dependence of macroscopic friction on rolling raises the question about the extent of the frictional laws derived from rock friction experiments. It is quite evident the need of rotational degrees of freedom in the continuum description of fault gouge. As deduced from the deformation field at the contacts, the Cosserat continuum approach should be consistent with the observed three phase separation of kinematic modes: (1) vorticity cells, where the Cosserat rotations are absent; (2) bearings given by antithetic couple of the Cosserat rotations, and therefore a pronounced rolling at the contacts; and (3) microbands of homothetic couples, with pronounced dislocations, and hence, strong accumulation of elastic energy and high frictional dissipation. This description requires an extension of the existing Cosserat continuum models, which consider only homothetic couples of the Cosserat rotations [19,20]. As far as dissipation is concerned, besides the Cauchy stress tensor, a couple stress tensor should be introduced as an additional static variable of the enhanced continuum, entering as the energetically dual counterpart of the gradient of the homothetic part of the Cosserat rotations [11,13,14,34]. In this context numerical simulations can be used as a virtual laboratory to assist the development of micromechanical constitutive models.

Concerning the heat flow paradox, we have shown that the rotational modes lead to a reduction of frictional dissipation of the same order as the fault gouge observations. However, our gouge model remains too simple and additional elements should be incorporated: pore fluid, particle shape and grain fragmentation. An important step forward will be the study of the contribution of grain fragmentation in the energy budget. Observations of fault zones suggest that earthquakes can pulverize rocks in the gouge [7]. This leads to a fractal grain size distribution and an increase of the gouge surface area. Therefore some additional issues concerning the heat flow paradox should be considered: Does fracture energy play an important role in the earthquake energy balance? Do such fractal gouges develop vortical structures and rotating bearings?

There are also some aspects about the aseismicity of fault zones which deserve detailed study in future work. Vortical structures and rotating bearings promote a coherent deformation which remains during two quakes. These may inhibit the large events we observe in samples with nonrotating grains. The dynamics of these rotational patterns will be significant in understanding the enigmatic aseismic creep, where two tectonic plates move against each other without accumulating elastic energy or generating earthquakes [35,36].

APPENDIX: RELATIONSHIP BETWEEN MACROSCOPIC FRICTION AND POWER DISSIPATION

In this section we use the energy balance to determine the connection between the average of power dissipation and the macroscopic friction coefficient of the shear cell in the critical state. The principle of energy conservation states that the change of internal energy is given by the work done by the external force minus the energy loss by the dissipative forces,

$$\frac{dE(t)}{dt} = F_n v_n(t) + F_t(t) v_t - P(t), \qquad \text{(A1)}$$

where E is the elastic potential energy stored at the contacts plus the total kinetic energy of the disks; F_n the constant normal force applied on the plates; $v_n(t)$ is the relative vertical velocity between the plates; $F_t(t)$ the tangential force applied on the plates; $v_t = 2v_0$ the constant relative tangential velocity between the plates; and $P(t)$ the work per unit of time done by the frictional forces.

Let us take the time average of Eq. (A1) along the critical state,

$$\left\langle \frac{dE(t)}{dt} \right\rangle = F_n \langle v_n(t) \rangle + \langle F_t(t) \rangle v_t - \langle P(t) \rangle. \tag{A2}$$

In the critical state, both potential and kinetic energy of the cell fluctuate around a constant value. This implies that

$$\left\langle \frac{dE(t)}{dt} \right\rangle \approx 0. \tag{A3}$$

Since void ratio fluctuates around a constant value in the critical state, the time averaged value of the normal compo-

nent of the relative velocity between the plates vanishes

$$\langle v_n(t) \rangle \approx 0. \tag{A4}$$

This, together with Eq. (A3) and the energy balance (A2) gives the connection between the friction coefficient (7) and the frictional power coefficient,

$$\langle P(t) \rangle = \mu_s F_n v_t. \tag{A5}$$

[1] P. Mora and D. Place, Geophys. Res. Lett. **26**, 123 (1999).
[2] J. Byerlee, Pure Appl. Geophys. **116**, 615 (1978).
[3] A. H. Lachenbruch and J. H. Sass, J. Geophys. Res. **97**, 4995 (1992).
[4] J. Sulem, I. Vardoulakis, H. Ouffroukh, M. Boulon, and J. Hans, Geosci. J. **336**, 455 (2004).
[5] J. Rice, J. Geophys. Res. **111**, B05311 (2006).
[6] R. Mahmoodi Baran, H. J. Herrmann, and N. Rivier, Phys. Rev. Lett. **92**, 044301 (2004).
[7] B. Wilson, T. Dewers, Z. Reches, and J. Brune, Nature (London) **434**, 749 (2005).
[8] A. Zervos, I. Vardoulakis, M. Jean, and P. Lerat, Mech. Cohesive-Frict. Mater. **5**, 305 (2000).
[9] J. A. Astrom, H. J. Herrmann, and J. Timonen, Phys. Rev. Lett. **84**, 638 (2000).
[10] C. T. Veje, D. W. Howell, and R. P. Behringer, Phys. Rev. E **59**, 739 (1999).
[11] W. Ehlers, E. Ramm, S. Diebels, and G. A. D'Addetta, Int. J. Solids Struct. **40**, 6681 (2003).
[12] I. Vardoulakis and J. Sulem, *Bifurcation Analysis in Geomechanics* (Blakie Academic and Professional, London, 1995), Chap. 8, pp. 281–283.
[13] F. Froiio and I. Vardoulakis, *Powders & Grains 2005* (Balkema, Leiden, 2005), pp. 135–139.
[14] H.-B. Mühlhaus and I. Vardoulakis, Geotechnique **37**, 271 (1987).
[15] W. Guenther, *Abhandlungen der Braunscheigschen Wissenschaftlichen Gesellschaft* (Boltze, Goettingen, 1958), Vol. 10, pp. 195–213.
[16] M. Satake, in *IUTAM Symposium on the Mechanics of Generalized Continua*, edited by F. Kroener(Springer-Verlag, Berlin, 1968), pp. 455–466.
[17] P. Papanastasiou and I. Vardoulakis, Int. J. Numer. Analyt. Meth. Geomech. **13**, 183 (1989).
[18] P. Lerat, Ph.D. thesis, ENPC, Champs-sur-Marne, France, 1996.
[19] P. Papanastasiou and I. Vardoulakis, Int. J. Numer. Analyt. Meth. Geomech. **16**, 389 (1992).
[20] J. Techman and E. Bauer, Comput. Geotech. **19**, 221 (1996).
[21] P. Mora and D. Place, PAGEOPH **143**, 61 (1994).
[22] S. Latham, S. Abe, and P. Mora, *Powders & Grains 2005* (Balkema, Leiden, 2005), pp. 213–217.
[23] M. P. Allen and D. J. Tildesley, *Computer Simulation of Liquids* (Oxford University Press, Oxford, 1987).
[24] T. Poeschel and T. Schwager, *Computational Granular Dynamics* (Springer, Berlin, 2004), Chap. 2.4, pp. 61–65.
[25] D. M. Wood, *Soil Behavior and Critical State Soil Mechanics* (Cambridge University Press, Cambridge, 1990).
[26] H. S. A. Murakami, H. Sakagushi, and T. Hasegawa, Soils Found. **37**, 123 (1997).
[27] M. R. Kuhn, Mech. Mater. **21**, 407 (1999).
[28] F. Radjai and S. Roux, Phys. Rev. Lett. **89**, 064302 (2002).
[29] P. R. Guduru, R. Ravichandran, and A. J. Rosakis, Phys. Rev. E **64**, 036128 (2001).
[30] H. M. Shodja and E. G. Nezami, Int. J. Numer. Analyt. Meth. Geomech. **27**, 403 (2003).
[31] M. R. Kuhn and K. Bagi, J. Eng. Mech. **130**, 826 (2004).
[32] K. Bagi and M. R. Kuhn, J. Appl. Mech. **71**, 493 (2004).
[33] I. Vardoulakis and J. Sulem, *Bifurcation Analysis in Geomechanics* (Blakie Academic and Professional, London, 1995).
[34] A. Tordesillas, S. D. C. Walsh, and B. S. Gardiner, BIT **44**, 539 (2004).
[35] C. H. Scholz, Nature (London) **391**, 37 (1998).
[36] T. I. Melbourne and F. H. Weeb, Science **300**, 1886 (2003).